Three-Dimensional Multipass SAR Focusing: Experiments With Long-Term Spaceborne Data

Gianfranco Fornaro, Fabrizio Lombardini, *Senior Member, IEEE*, and Francesco Serafino

***Abstract*—Synthetic aperture radar (SAR) interferometry is a modern efficient technique that allows reconstructing the height profile of the observed scene. However, apart for the presence of critical nonlinear inversion steps, particularly crucial in abrupt topography scenarios, it does not allow one to separate different scattering mechanisms in the elevation (height) direction within the ground pixel. Overlay of scattering at different elevations in the same azimuth-range resolution cell can be due either to the penetration of the radiation below the surface or to perspective ambiguities caused by the side-looking geometry. Multibaseline three-dimensional (3-D) SAR focusing allows overcoming such a limitation and has thus raised great interest in the recent research. First results with real data have been only obtained in the laboratory and with airborne systems, or with limited time-span and spatial-coverage spaceborne data. This work presents a novel approach for the tomographic processing of European Remote Sensing satellite (ERS) real data for extended scenes and long time span. Besides facing problems common to the airborne case, such as the nonuniformly spaced passes, this processing requires tackling additional difficulties specific to the spaceborne case, in particular a space-varying phase calibration of the data due to atmospheric variations and possible scene deformations occurring for years-long temporal spans. First results are presented that confirm the capability of ERS multipass tomography to resolve multiple targets within the same azimuth-range cell and to map the 3-D scattering properties of the illuminated scene.**

***Index Terms*—Multibaseline, multipass, synthetic aperture radar (SAR), three-dimensional (3-D) focusing, tomography.**

I. Introduction

SYNTHETIC aperture radar (SAR) focusing is a well-established operation for the generation of high-resolution two-dimensional (2-D) images of the scene backscattering properties. It exploits the coherent nature of the radiation transmitted by the active microwave system, to achieve a significant discrimination capability in the azimuth (along track) and range (cross track) directions [1], [2]. The high system phase stability is also the basis for interferometric applications, which have been significantly developed in the last decade.

Nevertheless, the reality is three-dimensional (3-D) and, either due to the intrinsic side-looking characteristic of the imaging system or to the penetration of the radiation below the surface, the resulting image represents only a projection (overposition) of the 3-D scene scattering properties along the elevation direction, usually referred to as normal-to-slant-range (nsr) direction, onto the 2-D azimuth-range plane.

SAR Interferometry (InSAR) is a technique that exploits two antennas, which image the scene from two slightly different look angles, to provide the reconstruction of the scene topography, i.e., the digital elevation model (DEM) [3], [4]. Key point of this technique is the determination of the off-nadir angle, on a pixel-by-pixel basis, of the effective phase center of the scatterers within the resolution cell. This information, in addition to the knowledge of the azimuth and range pixel coordinates provided by the SAR focusing operation, allows the complete localization of the (mean or dominant) scattering mechanism and therefore the reconstruction of the height surface. Differential interferometry (DInSAR) is a further advance of InSAR for the detection and mapping of ground deformations, which has considerably increased the use of SAR data in geophysics, hydrology, and in general for civilian and surveillance applications [5]–[7]. Nevertheless, in the case of multiple scattering occurring at different elevations, the distribution of the scatterers in the height direction is still underdetermined and cannot be resolved by two measurements, i.e., by a single baseline. Moreover, ambiguities may be still present, even in the case of surface scattering, due to layover effects caused by the side-looking geometry and steep topography.

Model-based polarimetric SAR interferometry was a first step toward the attempt to resolve multiple scattering in the height direction [8]. However, only specific types of scattering mechanisms, in particular those occurring in forested areas could be separated. Another technique for parameter estimation of forest layers is multifrequency-multibaseline SAR interferometry [9]. This technique is based on inversion of models of multiple interferometric observables from layered volumetric scatterers, such as interferometric phase and correlation in the various channels with frequency, look angle, baseline or polarization diversity, or a cross of them. Recently, model-based polarimetric interferometry has been experimented also over built-up areas [10].

Thanks to the recent advances of the space technology and the current planning for the next missions, who aim at involving

Manuscript received July 5, 2004; revised December 28, 2004. This work was supported in part by the Italian National Research Council L'Istituto di Elettronica e di Ingegneria dell'Informazione e delle Telecomunicazioni (CNR-IEIIT) and in part by the European Community on Provision 3.16 under the project of the Regional Center of Competence Analysis and Monitoring of the Environmental Risk.

G. Fornaro is with the Istituto per il Rilevamento Elettromagnetico dell'Ambiente (IREA), Consiglio Nazionale delle Ricerche (CNR), 80124 Napoli, Italy (e-mail: fornaro.g@irea.cnr.it).

F. Lombardini is with the Dipartimento di Ingegneria della Informazione, Università di Pisa, 56122 Pisa, Italy (e-mail: f.lombardini@iet.unipi.it).

F. Serafino is with the Dipartimento di Ingegneria Elettronica e Telecomunicazioni (DIET), Università di Napoli "Federico II," 80128 Napoli, Italy (e-mail: serafino.f@irea.cnr.it).

Digital Object Identifier 10.1109/TGRS.2005.843567

0196-2892/$20.00 © 2005 IEEE

Authorized licensed use limited to: Cyprus University of Technology. Downloaded on December 27,2025 at 18:41:27 UTC from IEEE Xplore. Restrictions apply.

constellations of cooperative, multipurpose satellites such as for instance, Cartwheel and similar [11], [12], the number of images relative to the same scene is expected to significantly grow in the future. Even with existing satellites, archives are filled by datasets, acquired at different times and with varying imaging geometries, over the same scene. For these reasons the current research is pushed toward the development of innovative processing techniques, aimed at jointly using, possibly in an optimal way, all the available information lying in the available data *cube* (*stack*) to produce new and/or more accurate physical measures.

With reference to the above methodological requirement, multipass DInSAR (M-DInSAR) is a first advance that has allowed setting up interferometric techniques able not only to detect and map surface deformations, but also to monitor their temporal evolution [13], [14]. This new technology has started substantial experimentations with real SAR data for civil protection services on volcanic and seismic areas, sliding monitoring, etc. Nevertheless, it is assumed that either a single dominant scattering mechanisms or closely distributed targets are present in the same azimuth-range cell.

Multibaseline (MB), or better, for available systems, multipass (MP) 3-D SAR focusing (3D-SAR), sometimes referred to as SAR tomography, constitutes a very recent advance with respect to SAR interferometry, that allows obtaining additional information from SAR data and overcoming the 2-D imaging limitation of available standard techniques. In fact, similarly to M-DInSAR, MP 3D-SAR is based on the multibaseline extension of the conventional, single baseline (single or repeat-pass) SAR Interferometry.

The basic principle of MP 3D-SAR is similar to the classical computer-aided X-ray tomography (CT) which was already used to explain SAR and InSAR systems (the only fundamental difference from CT being the coherent framework) [15]–[17]: the object is imaged by different looking angles to collect 3-D data and then the data stack is processed to convert the collected projections into a focused 3-D image. For the MP 3D-SAR case, instead of using polar-reformatting or backprojection techniques [18], processing is separated in two steps: the azimuth and range focusing for the 2-D high-resolution imaging, and the elevation inversion to achieve resolution capability in the third, nsr dimension. The first step is carried out via standard processing algorithms [1], [2]; the second step requires an additional pre-processing stage such as image coregistration and phase calibration as explained next.

Due to the fact that available spaceborne systems mainly operate at high frequencies [C-band for European Remote Sensing satellites (ERS) and RADARSAT], at the current state of the technology, MP spaceborne 3D-SAR allows mainly surface imaging. Nevertheless separation of multiple signal contributions for surface scattering in layover, such as mapping height in rough topography and urban areas, is possible. With airborne systems, operating at lower frequencies (L- or P-band) and at altitudes a few thousand meters high, MP 3D-SAR permits direct imaging of semitransparent media evidencing a volume scattering (forest, arid, and ice regions) thus allowing potential use in several fields such as geology, biomass estimation and monitoring and detection of buried structures for archeological and civil applications.

Moreover, with the current space technology, multiple baselines are obtained by using repeated passes; however, future mission planning, such as the European Space Agency Cartwheel, could allow obtaining single-pass multibaseline acquisitions.

Despite the fact that the interests in this field are currently growing, only a few contributions in the literature regard the application of SAR tomography to real data, whereas, most of the MP 3D-SAR works regard almost exclusively the development of advanced inversion algorithms [19]–[21]. First experiments with real data were carried out in laboratory with ideal experimental conditions [22] and using airborne systems [23], [24], whereas the application of tomography to spaceborne systems has been mainly limited to experiment on known corner reflectors and for small areas and limited time span [25], [26]. Notwithstanding, developments for spaceborne system would couple the potentials of tomography with the synoptic view of orbiting sensors, and could pave the way for future four-dimensional (4-D) (space–time) SAR imaging (differential tomography) [27].

With respect to CT, application of the MP 3D-SAR technique to real data is limited by a number of additional problems. First of all, the projections (focused SAR images) are not geometrically aligned. Second, typically only a relatively low number of passes is available [19], and they are commonly irregularly distributed in terms of spatial separation. The latter problem introduces a degree of ill conditioning in the inversion processing, following the 2-D SAR focusing operation, that may generate severe ambiguities in the elevation imaging [21]. Finally, spaceborne MP 3D-SAR acquisitions may generally span a time interval of several years. This fact, beside the introduction of an unavoidable temporal decorrelation, allows the appearance of disturbances due to atmospheric variations [28], [29] and to scene deformations that may significantly impair the quality of the 3-D reconstruction in terms of blurring and imaging ghosts [30].

Hence, due to the aforementioned problems, specific processing steps are required in the spaceborne case, before the application of the inversion procedure that allows reconstructing the elevation scattering profile. This preliminary processing aims at registering the images, and carrying out a space-varying phase compensation to allow eliminating both atmospheric and deformation contributions. Moreover, with respect to a simple beamforming inversion technique, the recent literature proposes a number of innovative techniques that allow moving from the focused, registered, and phase compensated data stack to the elevation scattering profile: they are either framed in the context of spectral estimation or of linear inverse problems [19]–[21]. Such approaches allow one, at least theoretically, to effectively overcome the limitations regarding the uneven baseline distribution and the limited number of images which cause poor resolution, high sidelobes, and leakage in the elevation (nsr) point spread function (PSF).

This work addresses the application of the MP 3D-SAR imaging to real spaceborne data toward an operational development of the technique. In particular, we show the result of an

Authorized licensed use limited to: Cyprus University of Technology. Downloaded on December 27,2025 at 18:41:27 UTC from IEEE Xplore. Restrictions apply.

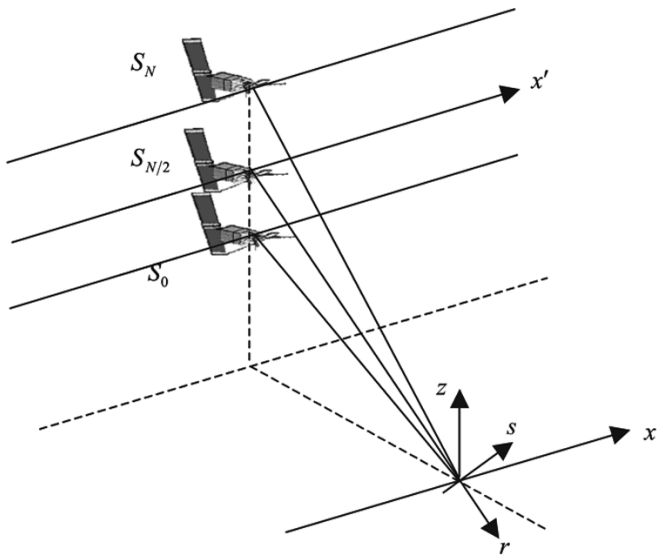

Fig. 1. Multipass acquisition geometry. For sake of simplicity, acquisitions are aligned along z.

experiment carried out with multipass ERS data over the area of Naples, consisting of 30 ERS images with a total orthogonal baseline span of about 1.1 km and a time span of about six years. The main aim of the work is to perceive the potentialities and the limits of the current MP 3D-SAR technique when applied to available spaceborne sensors. The operative frequency is in C-band, and therefore, the scattering takes place mainly at the surface level. Accordingly, our 3-D imaging allows achieving only a scattering separation in layover geometries, such as that occurring between ground and the buildings in urban areas.

The proposed work is an effort toward the development of innovative tools that allows enhancing the imaging capabilities of the ERS, ENVISAT, and other spaceborne SAR systems. Moreover, it could have important impact for multibaseline DInSAR monitoring, by allowing the separation of different scatterers in the same resolution cell, thus improving the percentage of imaged structures and detecting, in future, possible relative movements between buildings and ground.

In our experiment, we face all the aforementioned critical problems associated to real data processing. With respect to the work in [25] and [26], we achieve noticeable improvements in terms of scene coverage and percentage of imaged points at full resolution.

II. Three-Dimensional SAR Imaging Concept

This section briefly recalls the 3-D SAR imaging concept and two inversion methods: the beamforming based and the singular value decomposition (SVD)-based one: a more exhaustive analysis can be found in [21]. Let us refer to the geometry of the MP 3D-SAR system presented in Fig. 1: we have $N+1$ passes of the sensor in elevation direction, associated to the positions $S_0, \ldots, S_N$. Axes, x, r, z are the azimuth, range and height directions; s is the elevation or nsr direction. Antennas are supposed all flying in the x' direction and transmitting large bandwidth pulses along the range. Raw SAR data associated to the illuminated ground scene are collected in each pass; then, a classical focusing algorithm is applied to obtain 2-D full-resolution SAR images at each channel, usually referred to as single-look complex (SLC) images.

SLC images represent a "projection" along the elevation direction, i.e., onto the azimuth slant-range plane, of the illuminated 3-D scene backscattering properties. Letting x' and r' be the discrete variables associated to the azimuth and range position of the focused data, under the Born weak-scattering approximation the generic SLC data for the nth antenna is represented by the following form:

$$\hat{\gamma}_n(x', r') = \iint dx\, dr\, f(x' - x - \delta x, r' - r - \delta r) \times \int ds \gamma(x, r, s) \exp\left[-j\frac{4\pi}{\lambda} R_n(r, s)\right] \quad (1)$$

where λ is the operating wavelength, $R_n(s, r)$ represents the distance from the generic point target located at r and s coordinates on the ground and the sensor at the nth antenna (see Fig. 1), $n \in \{0, \ldots, N\}, \gamma(\cdot)$ is the function that models the 3-D (volumetric) scene scattering properties, and $\delta x(x, r)$ and $\delta r(x, r)$ are functions that account for the presence of a misregistration of the SLC images due to the different looking geometry in each pass. Moreover, all the integrals are extended to the illuminated volume and the first function in the integral argument is the so-called postfocusing (compressed) 2-D point spread function (PSF).

For the following, we assume that the focused images have been all coregistered with subpixel accuracy to the reference master antenna, say $n = N/2$, thus zeroing both δx and δr. Furthermore, the peakness of the PSF depends on the azimuth and range bandwidths of the SAR system: these are related to the synthetic aperture length and the transmitted bandwidth, respectively. Hereafter, we assume the bandwidth to be ideally infinite, thus allowing the postfocusing PSF to be approximated with a 2-D Dirac and primed and unprimed azimuth and range variables in (1) to represent the same entities. Under these assumptions, for each pixel (x, r), we collect a $N+1$ dimensional vector $\mathbf{g}_n$, whose generic element g_n is given by

$$g_n = \int_{-a}^{a} \gamma(s) \exp\left[-j\frac{4\pi}{\lambda}(R_n(s) - R_n(0))\right] ds \quad (2)$$

where the exponential factor highlights the application to the data of a so-called deramping compensation that aims at compensating the phase quadratic distortion of the received data, due to the Fresnel approximation; $2a$ is the extension, in the elevation direction, of the imaged scene.

By expanding the difference $R_n(s) - R_n(0)$ and by associating an inessential s-dependent term in the unknown backscattering function, we have

$$g_n = \int_{-a}^{a} \gamma(s) \exp[j2\pi\zeta_n s]\, ds \quad (3)$$

$$\zeta_n = \frac{2}{\lambda}\frac{b_{\perp n}}{r} \quad (4)$$

where $b_{\perp n}$ are the orthogonal baseline components of the passes with respect to the line of sight (los); see Fig. 2.

Authorized licensed use limited to: Cyprus University of Technology. Downloaded on December 27,2025 at 18:41:27 UTC from IEEE Xplore. Restrictions apply.

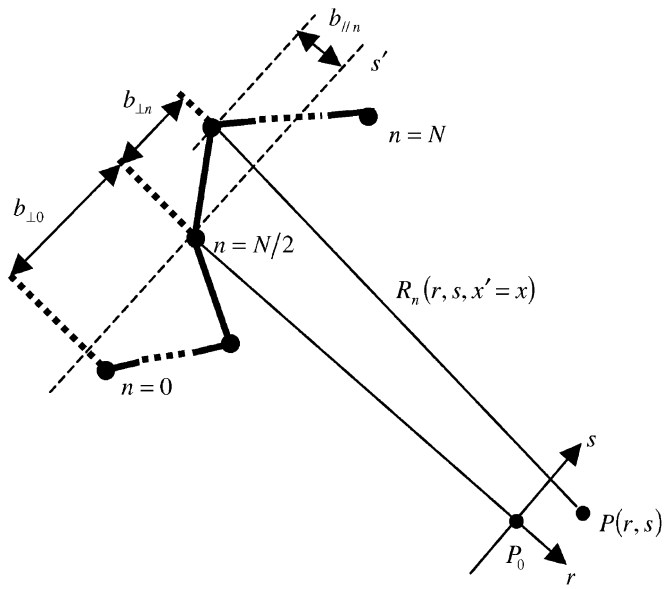

Fig. 2. Geometry in the zero Doppler plane, orthogonal to the azimuth direction.

According to basic concepts of electromagnetic theory, (3) and (4) illustrate the fundamental issue of the 3-D imaging stating that, but for a proper phase distortion compensation related to the fact that the object (scene) is located in the Fresnel region, the measured data represent samples of the spectrum of the unknown elevation scattering.

Collecting the received data in a vector $\mathbf{g}$, we easily recognize that the reconstruction problem of the unknown function $\gamma(s)$, with finite support $2a$, consists of inverting the following, finite rank semidiscrete compact operator L

$$\mathbf{g} = L\gamma \tag{5}$$

where the vector of the data points is assumed to belong to the Euclidean complex vector space $\mathrm{Y} \subseteq \mathcal{C}^{N+1}$. The unknown (object) function γ is assumed to belong to the Hilbert space of square integrable functions $\Gamma \subseteq L^2(-a, a)$: Y and Γ are often referred to as *data* and *unknown* spaces, respectively.

The factor a plays a key role in the imaging process as it changes the structure of the L operator. Its choice may modify the result of the inversion, thus allowing the inclusion of *a priori* information about the dimension along the nsr direction of the object to be reconstructed within the inversion algorithm. Under some conditions, and by properly handling possible ill-conditioning problems, proper tuning of a allows one to achieve finer resolutions in the resulting elevation reconstruction.

Although the real scene is continuous, the function γ, which is produced by the inversion procedure, is, obviously, discrete. Accordingly, let $\boldsymbol{\gamma}$ be the vector collecting, say, M uniformly spaced unknown samples. Equation (5) becomes

$$\mathbf{g} = \mathbf{L}\gamma \tag{6}$$

where $\mathbf{L}$ is an $(N+1) \times M$ matrix.

Several inversion techniques have been presented in the literature to invert the linear relation in (5) or (6); in the following, we focus on beamforming and SVD inversion, the latter being widely used in the context of linear inverse problems [31].

A. Beamforming

Assume $M = N + 1$ and the unknown samples to be spaced by a quantity

$$\Delta s = \frac{1}{N}\frac{\lambda r}{2b_\perp} = \frac{2s_{\max}}{N} \quad s_{\max} = \frac{\lambda r}{4b_\perp} \tag{7}$$

where $b_\perp$ is the mean baseline separation. In this case, the matrix L would be of the form

$$\mathbf{L} = [l_{nm}] \quad l_{nm} = \exp\left[j\frac{2\pi}{M}\frac{b_{\perp n}}{b_\perp}m\right]. \tag{8}$$

Beamforming inversion is then carried out via

$$\hat{\gamma} = \mathbf{L}^*\mathbf{g} \tag{9}$$

where $*$ denotes the Hermitian (conjugate transpose) operator. Explicitly, $\hat{\gamma}_n = \sum_n g_n \exp[-j(2\pi/M)(b_{\perp n}/b_\perp)m]$, where $\hat{\gamma}_n$ is the generic element of $\hat{\gamma}$. Note that for $b_{\perp n} = (n - N/2)b_\perp$ the inversion operator becomes a discrete Fourier transform (DFT) [32].

Performance of the beamforming may be typically poor in terms of resolution and high sidelobe ratio, especially in presence of highly uneven baseline distribution [32].

A solution to this problem could be obtained by interpolating the data $\mathbf{g}$ on a regular spectral grid [26]

$$\bar{\zeta}_n = \frac{2}{\lambda}\frac{b_\perp}{r} \tag{10}$$

by applying standard interpolation kernel. Following this data resampling, a standard DFT can be applied, possibly by zero padding the data to have $M \gg N+1$ to retrieve a reconstruction with a spacing of

$$\Delta s = \frac{1}{M-1}\frac{\lambda r}{2b_\perp} = \frac{2s_{\max}}{M-1}. \tag{11}$$

Unfortunately, performance is strongly dependent upon the choice of the interpolation kernel. A simple interpolation procedure, suitable to cases where the scene is mostly concentrated around a dominant target, can be devised by preliminary demodulation of the signal with respect to the dominant target that can be estimated via the nonuniform beamforming inversion in (6). More specifically, let us assume $\bar{s}$ to be the estimated elevation of the dominant target obtained by applying (9). Demodulation of $\mathbf{g}$, via a multiplication by a factor $\exp[-j2\pi\zeta_n\bar{s}]$, is carried out prior to the interpolation onto the regular grid (10) to apply simple low-pass interpolation procedures. The subsequent back multiplication by $\exp[j2\pi\zeta_n\bar{s}]$ allows locating the target back to the initial position and the application of a DFT allows completing the reconstruction process.

Authorized licensed use limited to: Cyprus University of Technology. Downloaded on December 27,2025 at 18:41:27 UTC from IEEE Xplore. Restrictions apply.

Note that the final resolution of beamforming cannot exceed the value

$$\delta r \approx \frac{\lambda r}{2B} = \frac{2s_{\max}}{N} \tag{12}$$

where $B = Nb_{\perp}$ is the total baseline span (Rayleigh limit). Moreover, performance of the interpolated beamforming is strongly dependent upon the concentration in elevation of the scattering mechanisms.

B. SVD Inversion

With respect to the beamforming reconstruction, this type of inversion is framed in the linear inversion framework [31] and has been recently proposed for MP 3D-SAR [21]. Here we summarize the main concepts.

By applying the SVD analysis, the semidiscrete operator L is amenable of a representation in terms of a singular system $\{\sigma_k, v_k(s), \mathbf{u}_k\}_{k=0}^{N}$, where σ_k are the eigenvalues of the system, v_k and $\mathbf{u}_k$ are the orthonormal base for the subspace of the *visible* (normal to *null-space*) objects and the orthonormal base for the *range* of the operator L, respectively. Introduction of the singular system allows us to write the following two fundamental relations that connect the data and the object function as follows:

$$\mathbf{g} = \sum_{k=0}^{N} \sigma_k \langle \gamma(s), v_k(s) \rangle_{\Gamma} \mathbf{u}_k \tag{13}$$

$$\gamma(s) = \sum_{k=0}^{N} \sigma_k^{-1} \langle \mathbf{g}, \mathbf{u}_k \rangle_{\mathrm{Y}} v_k(s). \tag{14}$$

Equations (13) and (14) represent the basic result of the SVD analysis. They state that, in principle, all the different vectors $\mathbf{u}_k$ concur in the composition of the observed vector $\mathbf{g}$: their contributions are however weighted by the singular values σ_k. In a real case, where data are corrupted by the noise, low singular values highlight critical directions, where the signal could be overwhelmed by the noise. Accordingly, should such directions being not identified and properly handled with, high instabilities in the inversion process could be observed. A way to achieve reliable reconstructions is to restrict the solution space by considering only the singular functions corresponding to singular values that lay above the noise level; the overall procedure is usually referred to as truncated SVD (TSVD).

The singular system in (13) and (14) is depending on the specification of $2a$ in (3), i.e., the size of the scene in the elevation direction. Allowing $2a$ to be independent of $2s_{\max}$, it gives us the possibility to consider available *a priori* information about the unknown support within the reconstruction algorithm. Therefore, beside the capability to avoid unreliable directions within the inversion process, SVD allows in some cases to reach superresolution imaging. The reader may refer to [21] for a more detailed discussion on this issue.

It is important to underline that, although the dimension of the acquired data is usually very large, each full resolution SAR image is indeed typically some thousand of pixels in both directions, the inversion of the L operator can be commonly made just once in the azimuth direction and recomputed only in range to account for the variations of the orthogonal baseline components due to the change of the looking geometry. In addition to this, the number of acquisitions is commonly not large; hence the computational cost of the reconstructing algorithm is not high.

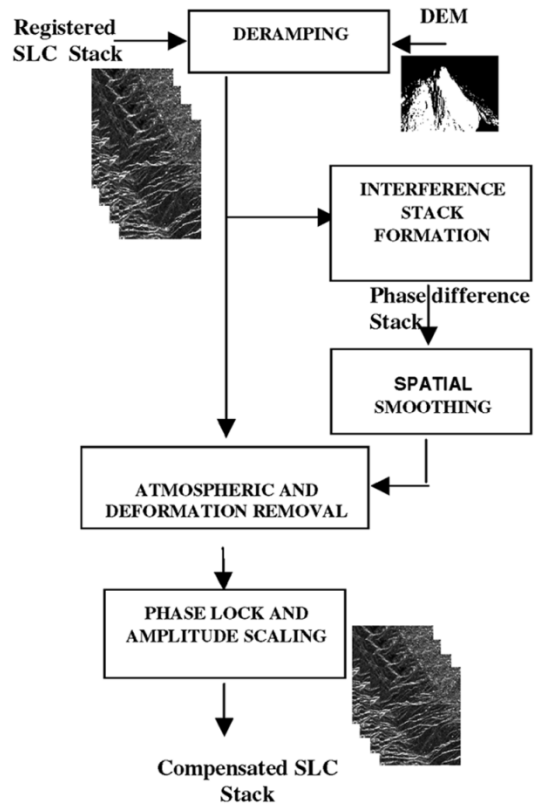

Fig. 3. Three-dimensional amplitude and phase compensation procedure.

III. Issues Related to Real Data Processing

So far, apart for accounting the case of unevenly distributed passes and for the problem of coregistering the SLC images, the analysis has been carried out in ideal conditions. Indeed, as pointed out also in the introduction, the real spaceborne data processing scenario is characterized by the appearance of a number of additional disturbances. Besides the presence of additive noise the data stack is calibrated neither in amplitude, nor in phase. Second, as data are acquired by using repeated passes with month-long separation and a years-long temporal span, atmospheric contributions as well as scene deformations may significantly ph[32]ase-modify the signal collected at the various antennas, in addition to possible complex reflectivity changes in areas of low temporal correlation. Compensation of the atmospheric and deformation phase variations is inherently space varying [28], [29], whereas temporal decorrelation is unaffordable unless the temporal span is drastically reduced such as for cooperative satellite clusters [11], [12].

With reference to Fig. 3, we start from the focused SLC image stack, ordered by orthogonal baselines, and we assume that a subpixel coregistration in the azimuth-range domain with respect to a common master image has been applied. A substantial dependence of the final target response stability on the accuracy of the coregistration step has been observed, especially with respect to the amplitude information.

Authorized licensed use limited to: Cyprus University of Technology. Downloaded on December 27,2025 at 18:41:27 UTC from IEEE Xplore. Restrictions apply.

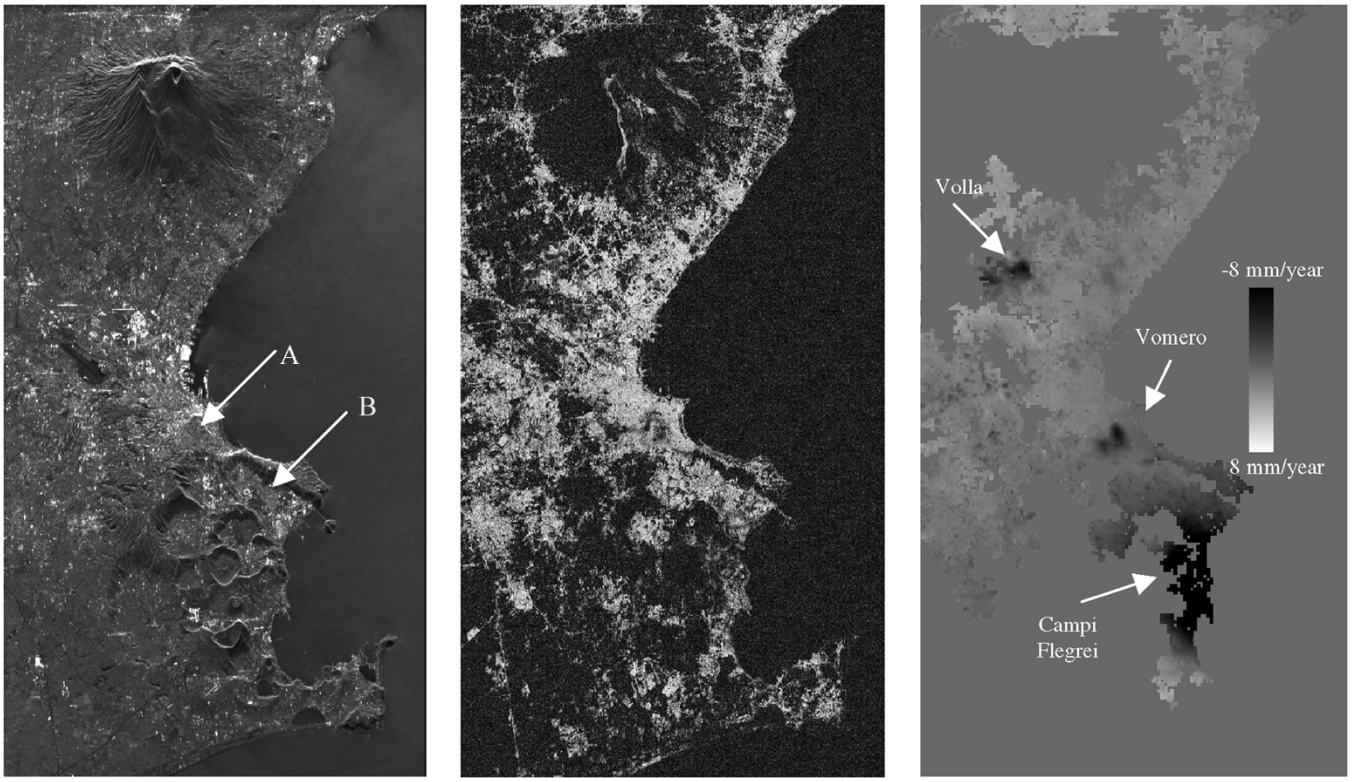

(a) (b) (c)

Fig. 4. (a) Multilook image of the processed area. (b) Multipass (temporal) coherence. (c) Estimated mean deformation velocity. Although the Campi Flegrei deformation reaches a value of 16 mm/year, the grayscale has been saturated to 8 mm/year to emphasize the other subsidence areas.

The first step of the 3D-MP SAR is the deramping operation: in our processing it is carried out starting form the orbit state vectors and with respect to a reference DEM. In particular, instead of compensating for the range distances $R_n(0)$ in (2) between the zero Doppler (nearest) position to a zero-elevation level at the midrange, we have updated in azimuth and range the reference elevation to the estimation given by the external DEM, i.e., for each image we subtracted the phase associated to $R_n(x, r, z = z(x, r))$. As a consequence, the resulting elevation (height) distribution of the tomographic reconstruction is aligned to the external DEM, in the sense that output elevation scattering profiling will be referred to the local topographic level. This operation, sometimes referred to as zero-baseline steering, allows us to carry out a fruitful demodulation of the signal for subsequent estimation.

The next step of the processing involves the space-varying phase compensation associated to atmospheric variations and to ground deformations. Whereas decorrelation introduces mostly high spatial frequency contributions, such phase distortions occur mainly at low spatial (azimuth and range) frequency: accordingly, they cannot be eliminated by simple local averages.

To outline the adopted filtering, we rewrite (3) also highlighting the explicit dependence on the azimuth and range coordinates

$$g_n(x,r) = A_n \int_{-a}^{a} \gamma(x,r,s) \exp\left[j4\pi \frac{b_{\perp n}}{\lambda r} s + j\varphi_d(n,x,r,s) \right] ds \exp[j\varphi_a(n,x,r)]. \quad (15)$$

In (15), A_n are complex constant factors in each image that embody the problem of amplitude and phase calibration losses, $\varphi_d(n,x,r,s)$ accounts for possible motion of the scatterer (x,r,s) occurring at the acquisition time n, whereas $\varphi_a(n,x,r)$ represents the atmospheric phase contribution in the nth pass at the (x,r) point. For the following, we assume that all the scatterers in the same azimuth-range pixel are possibly interested by the same deformation signal, i.e., we let

$$\varphi_d(n,x,r,s) = \varphi_d(n,x,r). \quad (16)$$

Accordingly, (15) can be rewritten as

$$g_n(x,r) = A_n \int_{-a}^{a} \gamma(x,r,s) \exp\left[j4\pi \frac{b_{\perp n}}{\lambda r} s \right] ds \times \exp[j\varphi_d(n,x,r) + j\varphi_a(n,x,r)]. \quad (17)$$

Atmospheric contributions occur mainly at low spatial and high temporal frequencies [29], whereas deformations generally take place at low spatial and low temporal frequency. We take the interference between successive images of the stack, thus building a phase difference stack which is then spatially low-passed to estimate both atmospheric variations and ground deformation changes over the adjacent antennas

$$\begin{aligned} \Delta\varphi_n(x,r) &= \arg\{lp[g_{n+1}(x,r) g_n^*(x,r)]\} \\ &= \Delta\varphi_d(n,x,r) + \Delta\varphi_a(n,x,r) + \Delta\varphi_t(n,x,r) \end{aligned} \quad (18)$$

Authorized licensed use limited to: Cyprus University of Technology. Downloaded on December 27,2025 at 18:41:27 UTC from IEEE Xplore. Restrictions apply.

TABLE I
MAIN PARAMETERS OF THE ERS SYSTEM

Distance from the scene center	r	848000 m
Mean uniform orthogonal baseline	$b_\perp$	36.7 m
Mean look angle	ϑ_0	23 °
Wavelength	λ	0.0565952 m
Number of acquisitions	*N+1*	30

with

$$\begin{aligned}\Delta\varphi_d(n,x,r) &= \varphi_d(n+1,x,r) - \varphi_d(n,x,r)\\ \Delta\varphi_a(n,x,r) &= \varphi_a(n+1,x,r) - \varphi_a(n,x,r)\\ \Delta\varphi_t(n,x,r) &= \varphi_t(n+1,x,r) - \varphi_t(n,x,r)\end{aligned} \tag{19}$$

where $lp[g_n(x,r)]$ is the low-pass spatial operator, and $\varphi_t(n,x,r)$ is the low-pass contribution of the integral in (17) related to residual topography contribution arising from smooth errors in the used external DEM.

Cumulating the phase in (18) along the stack, we extract the atmospheric and deformation distortion with respect to the master reference antenna $\varphi_n(x,r)$. The resulting phase stack is therefore subtracted from (17) thus giving

$$\begin{aligned}&g_n(x,r)\exp[-j\varphi_n(x,r)]\\ &\quad = A_n \int_{-a}^{a} \gamma(x,r,s)\exp\left[j4\pi\frac{b_{\perp n}}{\lambda r}(s-s_{\rm lp})\right]ds\end{aligned} \tag{20}$$

where according to the presence of residual topographic errors we let

$$\varphi_t(n,x,r) = \frac{4\pi}{\lambda}\frac{b_{\perp n}}{r}s_{\rm lp}. \tag{21}$$

Equation (20) shows that, but for the fact that the elevation distribution is now affected by the presence of the φ_t term, the obtained signal is deprived of the deformation and atmospheric contributions. Accordingly, the above filtering procedure allows us to achieve an elevation distribution that is referred to a local elevation described by the term $s_{\rm lp}$, which represents the elevation associated to the residual topography errors of the used DEM.

Note that both residual topography error and deformation signals can be estimated, independently of the subsequent 3-D processing, from the phase stack $\Delta\varphi_n(x,r)$ in (18) by applying pretty standard processing steps of the multipass DInSAR techniques [13], [14], [33]. Here we adopt an approach similar to that presented in [13] where phase variation analysis with respect to stable points, the celebrated permanent scatterers (PS), is carried out. However, in our case, we evaluate the mean temporal velocity and the residual topography variations on a pixel-to-pixel basis. Let $\arg[\Delta_x\Delta\varphi_n(x,r)]$ and $\arg[\Delta_r\Delta\varphi_n(x,r)]$ be the differential phase variation measured along the azimuth and the range, evaluated by interference on adjacent pixels on the low-pass signal $\mathrm{lp}[g_{n+1}(x,r)g_n^*(x,r)]$ in (18). Let also $\Delta_x v(x,r), \Delta_r v(x,r)\Delta_x s_{\rm lp}(x,r)\Delta_r s_{\rm lp}(x,r)$ be the azimuth and range variations of the mean temporal deformation velocity and residual topography: they can be estimated by maximizing the following temporal coherence operator:

TABLE II
USED ERS-1/ERS-2 DATA

Mission	Orbit	Day	Month	Year	$B_\perp$
ERS1	10201	28	6	1993	-493
ERS2	1894	31	8	1995	-456
ERS2	6904	15	8	1996	-447
ERS1	8197	8	2	1993	-446
ERS2	13417	13	11	1997	-431
ERS1	19563	12	4	1995	-427
ERS1	9700	24	5	1993	-420
ERS2	13918	18	12	1997	-374
ERS2	10912	22	5	1997	-331
ERS2	11914	31	7	1997	-293
ERS2	8908	2	1	1997	-289
ERS2	1393	27	7	1995	-85
ERS1	21066	26	7	1995	-50
ERS1	6694	26	10	1992	-25
ERS1	8698	15	3	1993	-19
ERS1	10702	2	8	1993	-19
ERS2	9409	6	2	1997	0
ERS2	17926	24	9	1998	30
ERS1	12205	15	11	1993	41
ERS1	4690	8	6	1992	98
ERS2	3397	14	12	1995	117
ERS1	11203	6	9	1993	130
ERS2	15922	7	5	1998	252
ERS1	7195	30	11	1992	259
ERS2	10411	17	4	1997	315
ERS2	5401	2	5	1996	409
ERS2	7906	24	10	1996	470
ERS1	25074	1	5	1996	500
ERS1	24072	21	2	1996	519
ERS2	2395	5	10	1995	572

$$\begin{aligned}&J(\Delta_x v(x,r), \Delta_x s_{\rm lp}(x,r))\\ &\quad = \sum_n \exp[j\Delta_x\Delta\varphi_n(x,r)]\exp\Big[-j\frac{4\pi}{\lambda}\Delta_x v(t_{n+1}-t_n)\\ &\qquad + j\frac{4\pi}{\lambda r_0}(b_{\perp n+1}-b_{\perp n})\Delta_x s_{\rm lp}\Big]\end{aligned} \tag{22}$$

and similarly for the range direction.

Note that, being independent among the different channels, effects of atmospheric variations are typically strongly mitigated in the summation operation; moreover, high baseline interferograms can be excluded from (22) to retain high spatial coverage. Estimated azimuth and range variations of the residual topography and velocity, i.e., $\Delta_x v(x,r), \Delta_r v(x,r)\Delta_x s_{\rm lp}(x,r)\Delta_r s_{\rm lp}(x,r)$, are then integrated in the LS sense to retrieve on a pixel basis the mean temporal velocity and the residual topography error.

As last remark, we note also that the hypothesis that possible deformations affect in the same way all the points in the same azimuth-range resolution cell is another key assumption in the above compensation procedure. However, considering particular variations of the temporal deformation characteristics (for instance, linear behavior) more complex procedures, referred

Authorized licensed use limited to: Cyprus University of Technology. Downloaded on December 27,2025 at 18:41:27 UTC from IEEE Xplore. Restrictions apply.

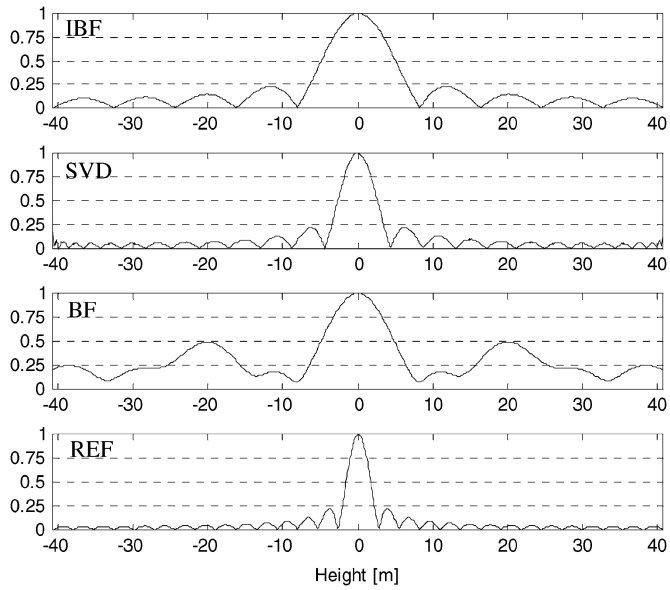

Fig. 5. Reference PSF with the real orthogonal baseline distribution obtained via the IBF, SVD, classical BF, and for a reference ideal acquisition (REF) with three times larger baseline span.

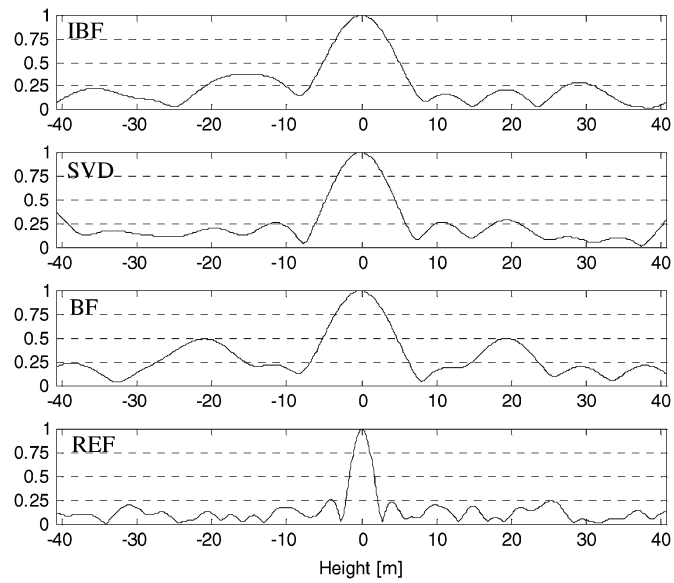

Fig. 6. As for Fig. 5 but with an additive noise with $\mathrm{SNR} = 2$ dB on the acquisitions.

to as differential-tomography or 4-D reconstruction procedures, aimed at separating different targets and deformations in the same resolution cell [27] could be adopted.

Final correction regards the absolute calibration of the images in the data stack. In particular, to accommodate possible (spatially constant) phase variations, we use a simple procedure based on locking the phase with respect to a reference single target. Moreover, by analyzing the amplitude response of stable targets, we both evaluate and compensate amplitude variations (data amplitude scaling) [13].

IV. Numerical Results

This section presents some results obtained by processing real data, acquired by the sensors ERS1-2, over the city of Naples, Italy, between 1992 and 1998. The system parameters are shown in Table I. We used 30 ($N = 29$) passes whose date and orthogonal baselines are summarized in Table II. The total baseline span B is about 1100 m and the theoretical resolution limit is 22 m in elevation, which corresponds to 8.7 m in height. Mean orthogonal baseline separation is 38 m, and thus the Nyquist elevation span, $2a_{\mathrm{nyq}}$, is 625 m, which corresponds to 244 m of total height span. Fig. 4(a) shows a multilook image of the investigated areas obtained by averaging the amplitude of the registered images. The Italian Geographical Military Institute (IGM) has provided the DEM used during the deramping: its accuracy is between 10 and 20 m.

Data have been focused and calibrated following the approach of Section III. Fig. 4(b) shows the (temporal) coherence image [13] evaluated along the stack, following the deramping operation and all the aforementioned amplitude and phase calibration steps. Bright points locate pixels where phase stability over the different acquisitions is observed, i.e., coherent targets where a single or a few closed scattering mechanisms occur. Black points correspond either to distributed targets in the elevation direction or to temporal decorrelated echoes. Fig. 4(c) shows the estimated mean velocity where subsidence areas in Campi Flegrei, Vomero, and Volla (around the Vesuvio Volcano) are easily identifiable.

A. Simulated Data

To understand the effects of the nonuniform baseline distribution within the inversion algorithm, we present in Fig. 5 the plot of the theoretical vertical PSF achievable by using the interpolated beamforming, the SVD and the classical (nonuniform) beamforming in absence of noise (i.e., residual miscalibrations and temporal decorrelation). From now on, one-dimensional profiles have been normalized to the amplitude peak. The scene size has been reduced (magnified) by a factor 3 with respect to the Nyquist size, i.e., we let $a = a_{\mathrm{Nyq}}/3$. We note the presence of high sidelobes due to the uneven spectral sampling in the nonuniform (conventional) beamforming (BF). The last plot in Fig. 5 shows the reference reconstruction (REF) we would have obtained in presence of uniform baseline distribution and a baseline span 3 times larger. Being in absence of noise, the SVD reconstruction allows achieving superresolution with respect to the interpolated beamforming (IBF). In Fig. 6 we have the same reconstruction of Fig. 5 but with the presence of additive noise. From Figs. 5 and 6, the interpolated beamforming, which is tuned to a single target, appears to have better performance with respect to the classical beamforming in terms of sidelobe ratio. However, this performance is strictly related to the fact that the interpolator has been tuned to a single target, and thus it exploits much *a priori* information. Indeed, limitations of the interpolated beamforming are evident when we consider more targets as reported in Fig. 7: SVD-based reconstruction gives good results in both cases.

The impact that atmospheric variations and possible scene deformation would have on classical beamforming has been also analyzed, to quantify the need for the space-varying phase compensation steps in spaceborne tomography. In particular, the effect of the random atmospheric signal on uncompensated

Authorized licensed use limited to: Cyprus University of Technology. Downloaded on December 27,2025 at 18:41:27 UTC from IEEE Xplore. Restrictions apply.

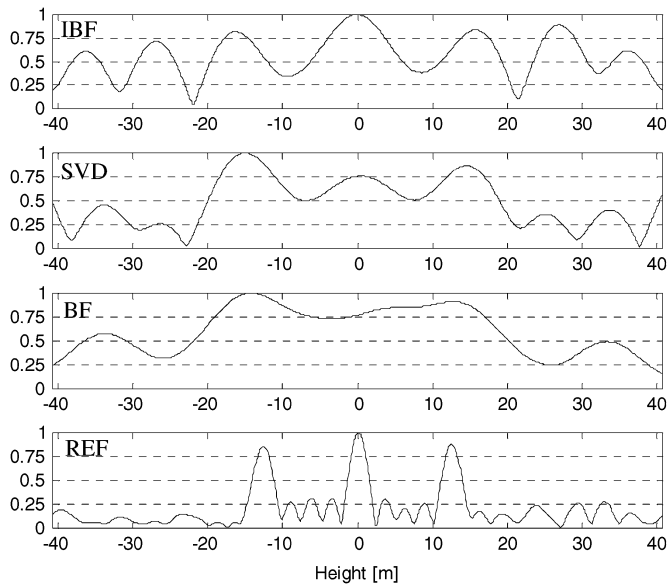

Fig. 7. As for Fig. 6 but with three targets.

classical beamforming has been analyzed by both simulation and analytical evaluation of the PSF obtainable on the average. Consider the beamforming intensity image

$$|\hat{\gamma}_n|^2 = \left|\sum_n g_{\mathrm{pa}}(n)\exp\left[-j\frac{2\pi}{M}\frac{b_{\perp n}}{b_\perp}m\right]\right|^2, \qquad (23)$$

where $g_{\mathrm{pa}}(n)$ are the elements of data vector $\mathbf{g}$ from a stable point target at zero elevation including atmospheric effects, and in practice zero padding can be used as in the interpolated beamforming $(M >> N+1)$. The average PSF is easily obtained as [30]

$$\begin{aligned} E\{|\hat{\gamma}_m|^2\} &= E\left\{\left[\sum_n g_{\mathrm{pa}}(n)\exp\left(-j\frac{2\pi}{M}\frac{b_{\perp n}}{b_\perp}m\right)\right]\right. \\ &\quad \cdot \left.\left[\sum_n g_{\mathrm{pa}}(n)\exp\left(-j\frac{2\pi}{M}\frac{b_{\perp n}}{b_\perp}m\right)\right]^*\right\} \\ &= N+1+2\sum_{n=1}^{N}\sum_{k=n+1}^{N+1}|R(n,k)| \\ &\quad \times\cos\left[\frac{2\pi}{M}\frac{b_{\perp n}-b_{\perp k}}{b_\perp}m+\angle R(n,k)\right] \end{aligned} \qquad (24)$$

where $(\cdot)^*$ denotes the conjugate operator, $R(n,k) = E\{g_{\mathrm{pa}}(n)g^*_{\mathrm{pa}}(k)\}$ is the autocorrelation of the point target signal affected by changes in atmospheric propagation, and signal power is assumed normalized to unity, $R(n,n) = 1$. Assuming Gaussian and temporal independent variations of the atmospheric path delay [34], signal autocorrelation can be expressed as [30], [35]

$$\begin{aligned} R(n,k) &= E\{g_{\mathrm{pa}}(n)g^*_{\mathrm{pa}}(n)\exp[j\Delta\varphi_a]\} \\ &= \int \exp(j\Delta\varphi_a)p(\Delta\varphi_a)\,d\Delta\varphi_a \\ &= \exp\left[-(4\pi/\lambda)^2\sigma_a^2\right], \qquad n \neq k \end{aligned} \qquad (25)$$

where $\Delta\varphi_a = \varphi_a(n) - \varphi_a(k)$ with unessential pixel coordinates dropped, $p(\Delta\varphi_a)$ is the Gaussian probability density function of the change of atmospheric phase contribution, and σ_a is the standard deviation (std) of the atmospheric one-way path delay.

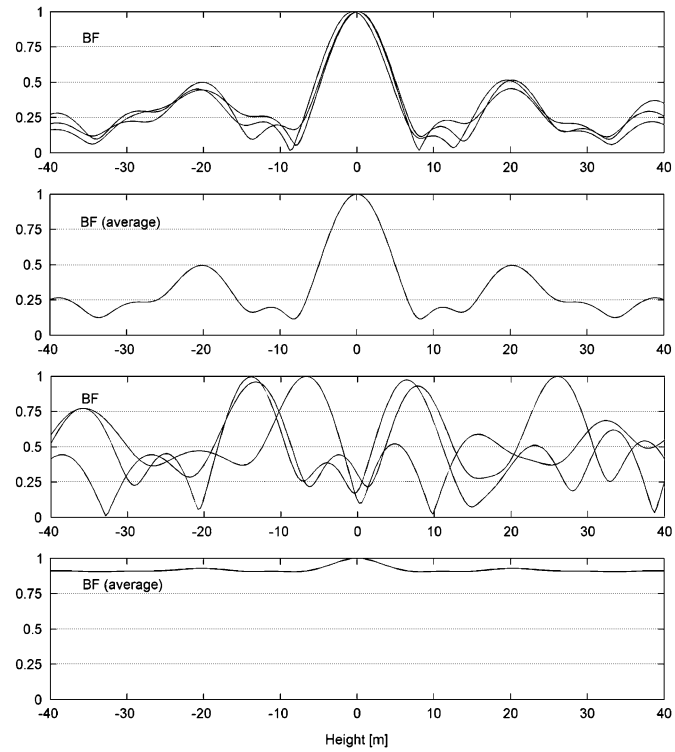

Fig. 8. Effects of an atmospheric one-way path delay of (top) 2 and (bottom) 10 mm std.

According to a few physical models and measurement campaigns, typical delay std ranges approximately from 1–20 mm [29], [34]. Delay changes are originated mostly from tropospheric water vapor differences [29], [34], convective clouds, rain, and storm fronts. The impact of atmospheric variations is apparent in the three sample simulation results in Fig. 8, for the baseline distribution of the real ERS data and one-way path delay std of 2 and 10 mm (0.04λ and 0.18λ, respectively). It is apparent how the small delay std does not drastically distort the sidelobe pattern of the nonuniform beamforming. Conversely, with a 10-mm delay std, the phase std almost reaches the value of π, which is enough to produce largely inflated sidelobes leading to heavy ambiguities. The corresponding average effect is also evaluated from (24) and (25) and shown in Fig. 8. A tolerable increase of relative peak sidelobe level of the average PSF results compared to unperturbed classical beamforming for 2 mm std. For 10 mm std, the PSF exhibits on the average an extremely high sidelobe level. It should be remarked that, following the phase compensation procedure of Section III, which benefits of the spatial correlation properties of the atmospheric phase contribution, quoted focusing losses are significantly reduced. Nevertheless, the above quantitative analysis can be applied to infer the imaging performance losses in presence of residual phase contributions due to partial atmospheric compensation.

Concerning the effect of scene deformation, it is worth noting that the baseline and temporal sampling sequences are not generally linearly related in multipass tomography. If the baselines were equispaced and sequentially and uniformly sampled in

Authorized licensed use limited to: Cyprus University of Technology. Downloaded on December 27,2025 at 18:41:27 UTC from IEEE Xplore. Restrictions apply.

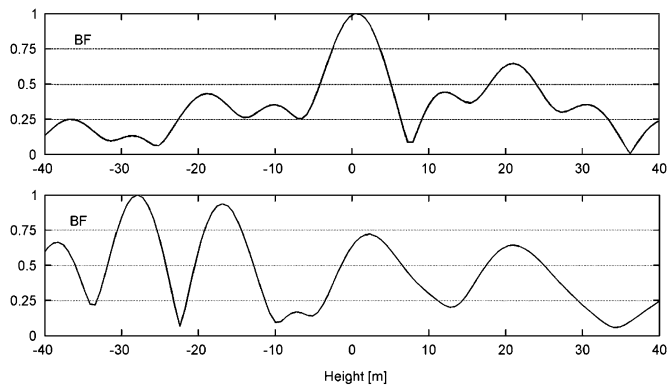

Fig. 9. Effects of a deformation with velocity (top) 2 and (bottom) 10 mm/year.

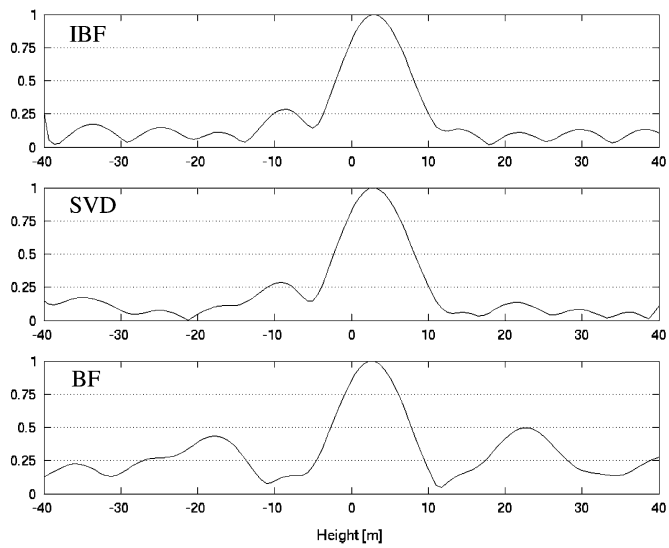

Fig. 10. Response of a single target versus the height in meters for real data [point A in Fig. 4(a)] obtained with IBF, SVD, and the classical BF.

time, the result of a uniform motion would be analogous to the well-known scatter misplacement effect in SAR imaging of moving targets, i.e., a mere shift in the elevation dimension in the tomographic problem at hand. Conversely, in practical tomographic data a time-linear backscatter phase history is viewed as highly nonlinear by the multibaseline array, because of the nonlinear and possibly nonmonotonic relationship between baselines and acquisition times [30]. This results in a completely different effect of uniform motion from classical SAR imaging, i.e., a PSF distortion. The impact of scene deformation has been analyzed for uniform motion and the baseline-time distribution of the real ERS data in Fig. 9, for velocity of 2 and 10 mm/year. Effect of 2 mm/year velocity is tolerable, while the velocity of 10 mm/year distorts significantly the PSF. In particular, quasi-grating lobes arise around height -28 and -17 m, masking the true point height and effectively reducing the unambiguous height range. These results confirm the sensitivity of spaceborne tomography to atmospheric variations and possible scene deformations.

B. Real Data

The PSF obtained on the phase-compensated real data, where apparently a single target is present, is shown in Fig. 10, which

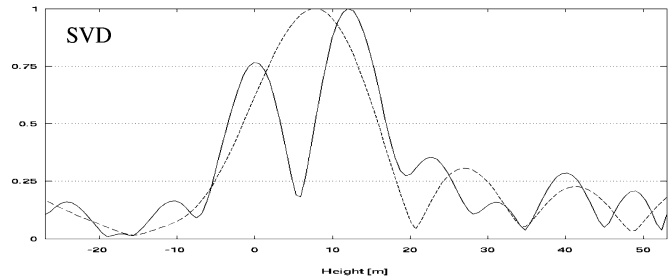

Fig. 11. Reconstruction of the point B in Fig. 4(a) with the SVD for (dotted line) a baseline span of 658 m and (continuous line) for a baseline span of 1063 m corresponding to a theoretical height resolution of about 14 and 8.7 m, respectively.

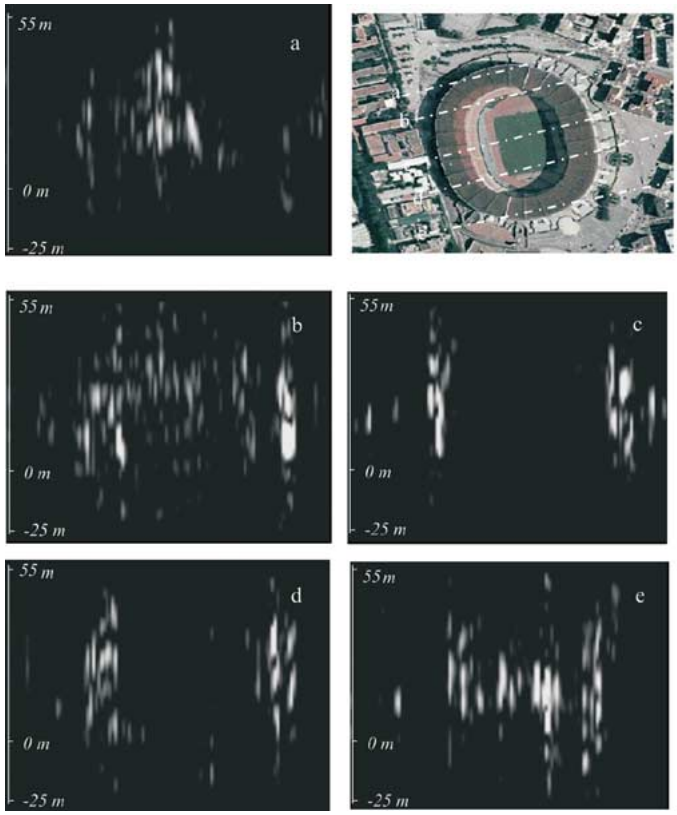

Fig. 12. Panels (a)–(e) represent azimuth-height sections of tomographic reconstruction over the San Paolo stadium in the subsiding Campi Flegrei area obtained with SVD. The top right image shows the orthophoto image of the same area (courtesy of CIRAM). Lines show the vertical sections.

is in good agreement with the ideal one in Fig. 5. This shows how effective is the proposed space-varying phase calibration.

Main advantage of 3-D focusing with respect to standard interferometry for the evaluation of the height of single target, is offered by the capability to distinguish between targets at different heights in the same spatial resolution cell. The processed dataset showed several pixels where multiple scattering mechanisms were present; for brevity reasons in the following we present only some of the key results. To emphasize the elevation resolution capability we applied, to a selected double scattering pixel, the SVD inversion algorithm with two different baseline spans.

In particular, the dot line plot in Fig. 11 shows the results achieved on the selected pixel when only the last 19 acquisitions of Table I are used, for a total orthogonal baseline span of

Authorized licensed use limited to: Cyprus University of Technology. Downloaded on December 27,2025 at 18:41:27 UTC from IEEE Xplore. Restrictions apply.

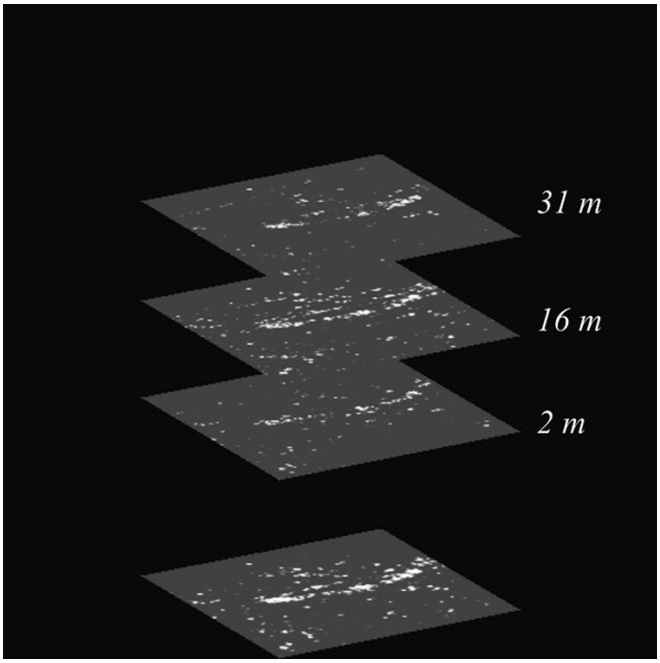

Fig. 13. Horizontal (azimuth-range) slices of the area of Fig. 12 obtained with the SVD. The original SAR image is on the bottom. Slices have been carried out at pixel 40, 62, and 84. The total number of pixels in height is 120.

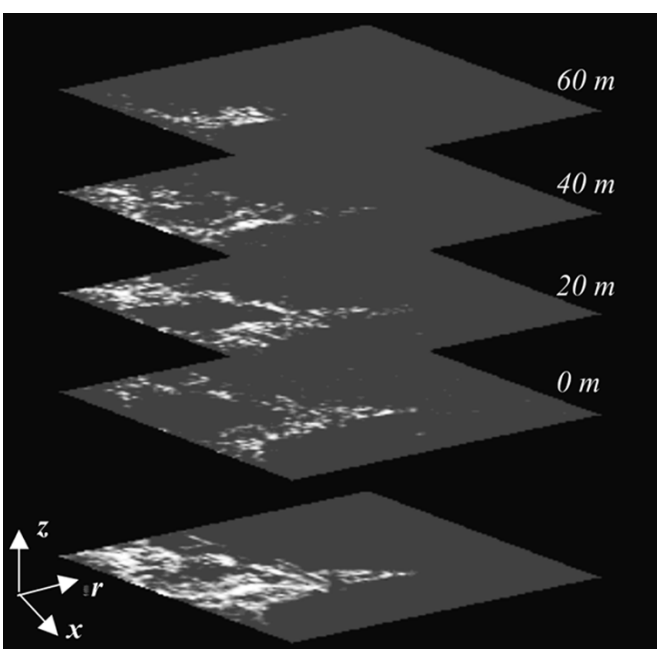

Fig. 14. Tomographic SVD reconstruction of the hilly area that starts from the Castel dell'Ovo, with the original SAR image on the bottom. Slices have been carried out at pixel 50, 80, 110, 140.

660 m. The theoretical resolution decreases to 14 m and only a single scatterer is detected. On the contrary, the continuous line in the same picture shows the case where all the available acquisitions are used in the SVD inversion. Now, obviously, the resolution is increased to its theoretical limit (7.1 m instead of 8.7 m as a consequence of a slight superresolution related to the selection of 11 useful eigenvalues; see [21]), and we are able to resolve the different targets, one of which is also dominant. Besides showing multiple scattering resolution capabilities of the system, this example also demonstrates consistency of the reconstructions obtained with different subarrays.

Fig. 15. Area of the hill of Posillipo. (Left) Orthopoto and (right) radar image.

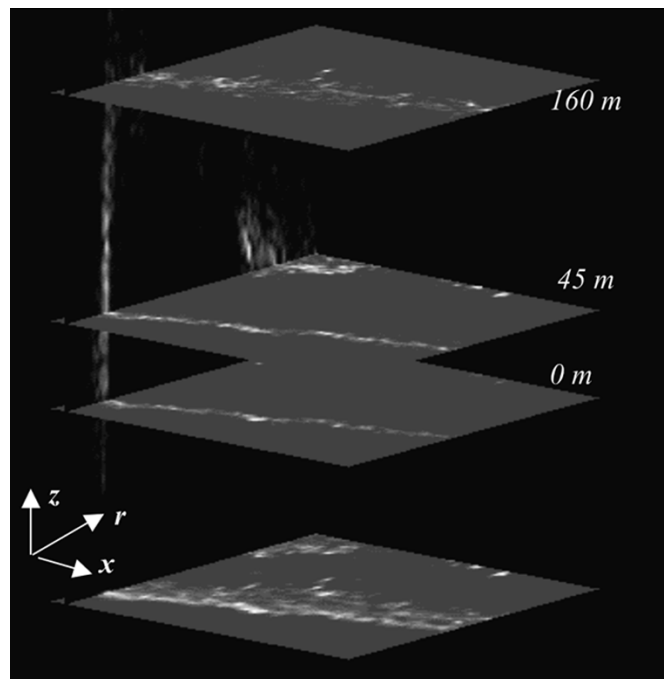

Fig. 16. Tomographic SVD reconstruction of the layover area related to hill of Posillipo. The slide in the center of the picture demonstrates that the hill has two main different slopes; x is the azimuth, r is the range, and z is the height.

In the following we address the reconstruction of an extended scene. In particular we consider the area of the San Paolo stadium which is a structure, with a metallic coverage, about 35 m height. Similarly to the previous plots we have "magnified" by a factor 3 the SVD reconstruction, i.e., we selected $a = 40$. The ortophoto image of the investigated area is shown in Fig. 12 (top right). Here we have drawn five segments associated with the azimuth-height sections carried out on the tomographic data and shown in the remaining subfigures. High radar cross-section scatterers can be located at the stadium flanks; these are due to the covering structure, built in 1990 for the soccer world championship. Topography variations are negligible in the area shown in the figures, and accordingly, we did not restore the topographic heights in the reconstruction. Although an overall confirmation of the structure size and height is evident, Fig. 13 shows horizontal sections (azimuth-range), carried out at different heights, here we clearly distinguish the whole structure of the stadium, which is the dominant structure in the area: the lower image is the original, elevation unfocused image.

Authorized licensed use limited to: Cyprus University of Technology. Downloaded on December 27,2025 at 18:41:27 UTC from IEEE Xplore. Restrictions apply.

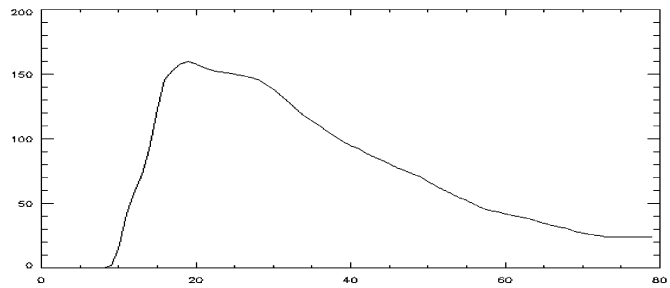

Fig. 17. Topography from the external DEM associated to the range-elevation section in Fig. 16. Height in meters versus the range pixel.

The next example shows the potential of the 3-D imaging in areas with nonnegligible topography variation. Accordingly we restored the topography variation in the obtained 3-D stack. Similarly to Fig. 13, Fig. 14 shows the horizontal sections with the original SAR image on the bottom. Here we can appreciate the capability of the 3-D MP-SAR system to separate the scattering in heights.

The last example considers the possibility to image layover areas, in this case we did not apply any magnification in the SVD reconstruction, thus letting $2a = 625$ m in elevation, i.e., about 240 m in height. In particular we consider the area of hill of Posillipo; see Fig. 15. Fig. 16 shows the azimuth-range sections at different heights of the 3-D reconstruction together with the original SAR image on the bottom and a range-elevation slice that shows layover effect. The topography associated to the range-elevation slice is shown in Fig. 17.

V. Conclusion

This work presented the results of a 3-D SAR focusing experiment carried out on real ERS repeat-pass data over the Bay of Napoli. With respect to short-term airborne tomography, processing of spaceborne data, where the signals can be acquired with passes repeated at temporal separations of the order of months, requires tackling a number of additional compensation problems. Although residual phase and amplitude instabilities due to coregistration errors and uncompensated phase distortions may be present in the processed data, presented experimental results clearly show that 3-D SAR focusing is a viable procedure to reconstruct the 3-D scattering properties of the observed scene also with spaceborne data. In particular, separation of multiple layover scatterers in C-band has been demonstrated. Future work shall be dedicated to spaceborne imaging of volumetric scatterers in L-band. Further developments concerning the improvement of existing processing techniques, which may suffer for the presence of multiple scattering mechanisms within the same resolution cell, such as multipass differential interferometry, can be foreseen as consequence of the presented experiment. Moreover, it represents a starting point for the future development of alternative or complementary nonlinear adaptive imaging methods [36] and 4-D, space–time, SAR processing [27] wherein the application of the SVD approach may give further improvement.

Acknowledgment

The authors would like to thank F. Soldovieri for interesting discussions on topics related to the inverse problem issue and P. Berardino for processing the orbital data and the reference DEM to provide the phase signals for the deramping step.

References

[1] J. C. Curlander and R. McDonough, *Synthetic Aperture Radar—System and Signal Processing*. New York: Wiley.
[2] G. Franceschetti and R. Lanari, Eds., *Synthetic Aperture Radar Processing*. Boca Raton, FL: CRC, 1999.
[3] G. Franceschetti and G. Fornaro, "Synthetic aperture radar interferometry," in *Synthetic Aperture Radar Processing*, G. Franceschetti and R. Lanari, Eds. Boca Raton, FL: CRC, 1999, ch. 4.
[4] R. Bamler and P. Hartl, "Synthetic aperture radar interferometry," *Inv. Probl.*, vol. 14, pp. R1–R54, 1998.
[5] K. Gabriel, R. M. Goldstein, and H. A. Zebker, "Mapping small elevation changes over large areas: Differential interferometry," *J. Geophys. Res.*, vol. 94, pp. 9183–9191, 1989.
[6] D. Massonnet, M. Rossi, C. Carmona, F. Ardagna, G. Peltzer, K. Feigl, and T. Rabaute, "The displacement field of the Landers earthquake mapped by radar interferometry," *Nature*, vol. 364, pp. 138–142, 1993.
[7] A. Borgia, R. Lanari, E. Sansosti, M. Tesauro, P. Berardino, G. Fornaro, M. Neri, and J. Murray, "Actively growing anticlines beneath Catania from the distal motion of Mount Etna's decollement measured by SAR interferometry and GPS," *Geophys. Res. Lett.*, vol. 27, pp. 3409–3412, Oct. 2000.
[8] S. R. Cloude and K. P. Papathanassiou, "Polarimetric SAR interferometry," *IEEE Trans. Geosci. Remote Sensing*, vol. 36, no. 5, pp. 1551–1565, Sep. 1998.
[9] R. N. Treuhaft, B. E. Law, G. P. Asner, and S. Hensley, "Vegetation profile estimates from multialtitude, multifrequency radar interferometric, and polarimetric data," in *Proc. IGARSS*, Jul. 2000, pp. 126–128.
[10] S. Guillaso, L. Ferro-Famil, A. Reigber, and E. Pottier, "Analysis of built-up areas from polarimetric interferometric SAR images," in *Proc. IGARSS.*, Toulouse, France, Jul. 2003, pp. 1727–1729.
[11] D. Massonnet, E. Thouvenot, S. Ramongassie, and L. Phalippou, "A wheel of passive radar microsats for upgrading existing SAR projects," in *Proc. IGARSS*, vol. 3, Honolulu, HI, 2000, pp. 1000–1003.
[12] R. Bamler, M. Eineder, B. Kampes, H. Runge, and N. Adam, "SRTM and beyond: Current situation and new developments in spaceborne INSAR," in *Proc. ISPRS*, Hannover, Germany, 2001.
[13] A Ferretti, C. Prati, and F. Rocca, "Nonlinear subsidence rate estimation using permanent scatterers in differential SAR interferometry," *IEEE Trans. Geosci. Remote Sens.*, vol. 38, no. 5, pp. 2202–2212, Sep. 2000.
[14] P. Berardino, G. Fornaro, R. Lanari, and E. Sansosti, "A new algorithm for surface deformation monitoring based on small baseline differential SAR interferograms," *IEEE Trans. Geosci. Remote Sens.*, vol. 40, no. 11, pp. 2375–2383, Nov. 2002.
[15] D. C. Munson, J. D. O'Brien, and W. K. Jekins, "A tomographic formulation of spotlight mode synthetic aperture radar," *Proc. IEEE*, vol. 62, no. 8, pp. 917–925, Aug. 1983.
[16] V. Jakowatz, D. E. Wahl, P. H. Eichel, D. C. Ghiglia, and P. A. Thompson, *Spotlight-Mode Synthetic Aperture Radar: A Signal Processing Approach*. Boston, MA: Kluwer, 1996.
[17] N. Marechal, "Tomographic formulation of interferometric SAR for terrain elevation mapping," *IEEE Trans. Geosci. Remote Sens.*, vol. 33, no. 3, pp. 726–739, May 1995.
[18] M. D. Desai and W. K. Jekins, "Convolution backprojection image reconstruction for spotlight mode synthetic aperture radar," *IEEE Trans. Geosci. Remote Sensing*, vol. 30, no. 4, pp. 505–515, Jul. 1992.
[19] J. L. H. Webb and D. C. Munson Jr., "Radar imaging of three-dimensional surfaces using limited data," in *Proce. IEEE Int. Conf. Image Processing*, Washington, DC, Oct. 1995, pp. 136–139.
[20] F. Gini, F. Lombardini, and M. Montanari, "Layover solution in multibaseline SAR interferometry," *IEEE Trans. Aerosp. Electron. Syst.*, vol. 38, no. 4, pp. 1344–1356, Oct. 2002.
[21] G. Fornaro, F. Serafino, and F. Soldovieri, "Three dimensional focusing with multipass SAR data," *IEEE Trans. Geosci. Remote Sens.*, vol. 41, no. 4, pp. 507–517, Apr. 2003.
[22] P. Pasquali, C. Prati, F. Rocca, and M. Seymour, "A 3D SAR experiment with EMSL data," in *Proc. IGARSS*, Firenze, Italy, 1995, pp. 784–786.
[23] A. Reigber and A. Moreira, "First demonstration of airborne SAR tomography using multibaseline L-band data," *IEEE Trans. Geosci. Remote Sens.*, vol. 38, pp. 2142–2152, Sep. 2000.
[24] C. V. Jakowatz and D. E. Wahl, "Three-dimensional tomographic imaging for foliage penetration using multiple-pass spotlight-mode SAR," presented at the *35th Asilomar Conf. Signal Systems and Computers*, 2001.
[25] J. Homer, I. D. Longstaff, Z. She, and D. Gray, "High resolution 3-D imaging via multi-pass SAR," *Proc. Inst. Elect. Eng., F*, vol. 149, no. 1, pp. 45–50, Feb. 2002.

Authorized licensed use limited to: Cyprus University of Technology. Downloaded on December 27,2025 at 18:41:27 UTC from IEEE Xplore. Restrictions apply.

[26] Z. She, D. A. Gray, R. E. Bogner, J. Homer, and I. D. Longstaff, "Three-dimensional spaceborne synthetic aperture radar (SAR) imaging with multipass processing," *Int. J. Remote Sens.*, vol. 23, pp. 4357–4382, Oct. 2002.

[27] F. Lombardini, "Differential tomography: A new framework for SAR interferometry," in *Proc. IGARSS*, Toulouse, France, Jul. 2003, pp. 1206–1208.

[28] H. A. Zebker, P. A. Rosen, and S. Hensley, "Atmospheric effects in interferometric synthetic aperture radar surface deformation and topographic maps," *J. Geophs. Res.*, vol. 102, pp. 7547–7563, 1997.

[29] R. Hanssen, D. Moisseev, and S. Businger, "Resolving the acquisition ambiguity for atmospheric monitoring in multi-pass radar interferometry," in *Proc. IGARSS*, Toulouse, France, Jul. 2003, pp. 1202–1205.

[30] F. Lombardini and H. D. Griffiths, "Effects of temporal decorrelation on 3-D SAR imaging using multiple pass beamforming," in *Proc. IEE EUREL Meeting on Radar and Sonar Signal Processing*, Peebles, U.K., Jul. 1998, pp. 34/1–34/4.

[31] F. M. Bertero, "Linear inverse and ill-posed problems," in *Advances in Electronics and Electron Physics*. Orlando, FL: Academic, 1989.

[32] P. Stoica and R. L. Moses, *Introduction to Spectral Analysis*. Upper Saddle River, NJ: Prentice-Hall, 1997.

[33] B. M. Kampes and N. Adam, "Velocity field retrieval from long term coherent points in radar interferometric stacks," in *Proc. IGARSS*, vol. 2, Toulouse, France, Jul. 2003, pp. 941–943.

[34] J. M. Sabater, R. Hanssen, B. M. Kampes, A. Fusco, and N. Adam, "Physical analysis of atmospheric delay signal observed in stacked radar interferometric data," in *Proc. IGARSS*, Toulouse, France, Jul. 2003, pp. 2112–2115.

[35] H. A. Zebker and J. Villasenor, "Decorrelation in interferometric radar echoes," *IEEE Trans. Geosci. Remote Sens.*, vol. 30, no. 5, pp. 950–959, Sep. 1992.

[36] F. Lombardini and A. Reigber, "Adaptive spectral estimation for multibaseline SAR tomography with airborne L-band data," in *Proc. IGARSS*, Toulouse, France, Jul. 2003, pp. 2014–2016.

Gianfranco Fornaro received the laurea degree in electronic engineering and the Ph.D. degree from the University "Federico II," Naples, Italy, in 1992 and 1997, respectively.

Since 1996, he has been with the Istituto per il Rilevamento Elettromagnetico dell'Ambiente (IREA), Italian National Research Council (CNR), Naples, where he is currently a Senior Researcher. He was an Adjunct Professor of signal theory and communication at the University of Napoli "Federico II," University of Cassino, and University Reggio Calabria. His main research interests are in the signal processing field with applications to SAR data processing from airborne and spaceborne systems, including motion compensation, multichannel SAR Interferometry, differential SAR interferometry, and 3-D SAR focusing. He has been a Visiting Scientist with the German Aerospace Establishment (DLR) and the Politecnico of Milano, and he has been a Lecturer in several universities and international institutions such as the Istituto Tecnologico de Aeronautica (ITA), Sao José dos Campo, Brazil, and RESTEC, Tokyo, Japan. He is currently Responsible of the Remote Sensing Unit of the Regional Center of Competence "Analysis and Monitoring of the Environmental Risk." He is a Guest Co-Editor of the EURASIP *Journal of Applied Signal Processing* special issue on Advances in Interferometric SAR Processing.

Dr. Fornaro was awarded the Mountbatten Premium by the Institution of Electrical Engineers (IEE) in 1997.

Fabrizio Lombardini (M'93–SM'03) received the laurea degree (with honors) in electronic engineering and the Ph.D. degree in telecommunication engineering from the University of Pisa, Pisa, Italy, in 1993 and 1997, respectively.

In 1997, he was granted by the European Union a Marie Curie Fellowship of the Training and Mobility of Researchers (TMR) Program, which he spent as a Postdoctoral Researcher with the Department of Electronic and Electrical Engineering, University College London, London, U.K., from 1998 to 1999. Then, he joined the Department of Information Engineering, University of Pisa, where he is currently an Assistant Professor. He has given lectures at universities and institutions in Italy and abroad. He is coauthor of a tutorial entitled "Multibaseline Post-processing for SAR Interferometry," which was presented at the IEEE Sensor Array and Multichannel Workshop (July 2004). His general interests are in the areas of statistical signal processing, estimation and detection theory, adaptive and superresolution spectral analysis, array processing, and performance bounds evaluation, with application to radar systems. In particular, his research interests include multibaseline and multifrequency interferometric SAR algorithms and systems, both cross- and along-track, multibaseline SAR tomography, multisensor data fusion, and radar detection in non-Gaussian clutter. He is a Guest Co-Editor of the EURASIP *Journal of Applied Signal Processing* special issue on Advances in Interferometric SAR Processing

Dr. Lombardini has chaired two special sessions at international conferences.

Francesco Serafino received the laurea degree in electronic engineering from the University Reggio Calabria, Calabria, Italy, and the Ph.D. degree from the University "Federico II," Naples, Italy, in 2000 and 2005, respectively.

He collaborated with the Istituto per il Rilevamento Elettromagnetico dell'Ambiente (IREA), an Institute of the Italian National Research Council (CNR). His main research interests are in the spotlight SAR data processing area, SAR interferometry, and differential SAR interferometry.

Authorized licensed use limited to: Cyprus University of Technology. Downloaded on December 27,2025 at 18:41:27 UTC from IEEE Xplore. Restrictions apply.